Examining the magnetic geometry of magnetic flux rope: from the view of single-point analysis

Chi Zhang[1,2], Zhaojin Rong[1,2,3], Chao Shen[4], Lucy Klinger[5], Jiawei Gao[1,2], James A. Slavin[6], Yongcun Zhang[7], Yong Wei[1,2,3], and Weixing Wan[1,2,3]

[1]Key Laboratory of Earth and Planetary Physics, Institute of Geology and Geophysics, Chinese Academy of Sciences, Beijing, China

[2]College of Earth Science, University of Chinese Academy of Sciences, Beijing, China

[3]Beijing National Observatory of Space Environment, Institute of Geology and Geophysics, Chinese Academy of Sciences, Beijing, China

[4]Harbin Institute of Technology, Shenzhen, China

[5]Beijing International Center for Mathematical Research, Peking University, China

[6]Department of Climate and Space Sciences and Engineering, University of Michigan, Ann Arbor, MI, USA

[7]State Key Laboratory of Space Weather, National Space Science Center, Chinese Academy of Sciences, Beijing, China

Corresponding author: Zhaojin Rong (rongzhaojin@mail.iggcas.ac.cn)

Key Points:

- A magnetic flux rope of ion-scale observed by MMS is studied by multiple analysis methods.
- We demonstrated that the flux rope's geometry can be reliably inferred by the single-point method developed by Rong et al. [2013].
- The method of Rong et al., [2013] can be applied widely to studies of flux rope that use single-point spacecraft missions.

Abstract

With Magnetospheric Multiscale Mission (MMS) observation of a magnetic flux rope of ion scale in magnetopause, we apply the single-point method presented by Rong et al., [2013] to study the magnetic field structure of flux rope. The calculated geometric parameters, e.g. axis orientation, helical handedness, current density, curvature radius, and boundaries of flux rope show well consistency with those derived from the multi-point methods. Thus, the single-point method of Rong et al., [2013] is reliable for studying the interior field structure of magnetic flux rope and could be applied widely to single-point spacecraft missions that examine the dynamics of flux rope.

Plain Language Summary

Magnetic flux ropes, characterized as magnetic field lines that wrap and rotate around a central axis, are observed ubiquitously in the space environment. Magnetic flux ropes are usually seen as the products of magnetic reconnection that releases magnetic field energy explosively. An accurate determination of the flux rope's geometric parameters (e.g. axis orientation, current density, curvature radius, boundaries) is important for studying its geometry and exploring its origin and evolution. In principle, these geometric parameters can be addressed and derived by a four-point analysis of Cluster or MMS tetrahedron. However, most spacecraft missions are single-point measurements, thus limiting the application of multi-point analysis. A single-point method that infers the axis orientation of flux rope was recently developed by Rong et al. [2013]. Compared to multi-point analysis methods that study a flux rope case observed by MMS tetrahedron, we show the method of Rong et al. [2013], apart from axis orientation, can reasonably infer the current density, helical handedness, curvature radius, and boundaries of flux rope. Thus, it seems worthwhile to apply widely this single-point method by Rong et al. [2013]

to single-point spacecraft missions for the purpose of examining the geometry and dynamics of flux ropes.

1 Introduction

Magnetic flux rope (MFR), manifested as helical magnetic field lines wrapping around an axis, has been observed ubiquitously in the space plasma environment, e.g. Earth's magnetotail [e.g., Slavin et al., 2003a, 2003b; Zhang et al., 2007; Yang et al., 2014; Sun et al., 2019], Earth's magnetopause [e.g., Russel and Elphic, 1979; Eastwood et al., 2016; Akhavan-Tafti et al., 2018], Martian magnetotail [Hara et al., 2017], Venusian magnetotail [Zhang et al., 2012], Mercury's magnetotail [e.g., Dibraccio et al., 2015; Zhao et al., 2019], and interplanetary space [e.g., Burlaga, 1988; Lepping et al., 1990]. MFR is generally considered as a product of magnetic reconnection that releases magnetic field energy explosively [e.g., Eastwood et al., 2016; Hones, 1977; Schindler, 1974; Wang et al., 2015; Zhou et al., 2017].

Accurate estimation of the axis orientation of MFR is vital for determining the magnetic geometry of MFR and exploring its origin and evolution. This issue could well be solved by the multi-point analysis with the advent of multi-spacecraft missions, e.g. Cluster mission [Escoubet et al., 2001] and Magnetospheric Multiscale mission (MMS) [Burch et al., 2015]. The multi-point methods developed so far, such as Minimum Directional Derivative (MDD) [Shi et al., 2005; Shi et al., 2019], Multiple Triangulation Analysis (MTA) [Zhou et al., 2006], and Magnetic Rotation Analysis (MRA) [Shen et al., 2007] can derive the axis orientation by analyzing the spatial gradient of the magnetic field. However, most current spacecraft missions, such as Geotail [Nishida et al., 1994], do not have the unique tetrahedron configuration like Cluster or MMS, and thus face a great challenge in inferring the axis orientation of MFR.

In the past, several popular single-point methods have attempted to infer the axis orientation. (1) The minimum variance analysis based on magnetic field (BMVA) [Sonnerup and Scheible, 1998]. It was argued that BMVA can infer the axis orientation relying on the calculated orthogonal eigen directions of magnetic field variation. However, the tests showed that the inferred axis orientation critically depends on the spacecraft's crossing trajectory [Moldwin and Hughes, 1991; Burlaga, 1988; Xiao et al., 2004; Rong et al., 2013]; (2) The fit of force-free model [e.g. Lundquist, 1950; Lepping et al., 1990; Eastwood et al., 2016]. One cannot guarantee that the detected real field structure of MFR always fits well with the force-free model. Multi-point analysis of Cluster demonstrated that only the field structure around MFR's center is close to the force-free field [e.g. Yang et al., 2014]; (3) The technique of Grad-Shafranov (GS) reconstruction [Hau and Sonnerup, 1999; Hu and Sonnerup, 2002]. For the GS technique, MFR is assumed to be in approximate magnetohydrostatic equilibrium, and a trial scheme is performed repeatedly to search for the axis orientation, for which the curve for total transverse pressure (plasma pressure plus magnetic pressure) versus the magnetic vector potential in the inbound crossing should ideally be equal to that of the outbound crossing. This method may yield a reasonable solution of axis orientation, but at the expense of a trial scheme.

Recently, based on an assumption of azimuthal symmetry of MFR's helical field, Rong et al., [2013] presented a simple single-point method (we refer to it as R13) to derive the axis orientation of MFR. Application to the same MFR cases by the four spacecraft of Cluster demonstrated that this method could infer the axis orientation consistently without restriction of force-free field configuration. Nonetheless, the typical separation scale of Cluster tetrahedron is about several hundred kilometers to thousands of kilometers, which is comparable to or larger than the typical scale of MFR observed in magnetosphere. The multi-point analysis of Cluster on

95 the field structure of MFR could yield significant truncation error owing to the large separation
96 scale [e.g. Shen et al., 2003, 2007]. Therefore, Rong et al. [2013] did not make the direct
97 comparison between R13 and the multi-point analysis of Cluster.

98 The closely separated four spacecraft (separation scale 10~20 km) of MMS tetrahedron
99 [Burch et al., 2015], with unprecedented temporal and spatial resolutions measurements of
100 magnetic field and plasma, make it possible to evaluate the validity of R13 by comparison with
101 the multi-point analysis. The high-resolution of magnetic field is measured by a fluxgate
102 magnetometer operating at 128 vectors per second in burst-mode [Russell et al., 2014]. While
103 FPI (Fast Plasma Investigation) onboard MMS can measure the electrons at a burst cadence of
104 30ms and ions at a burst cadence of 150 ms, with an energy/charge range from 10 eV/q to 30000
105 eV/q. [Pollock et al., 2016]. The plasma moments are derived from the all-sky electron and ion
106 distributions by FPI.

107 As a continuation of Rong et al., [2013], by comparison with multi-point analysis methods
108 in analyzing a flux rope case observed by MMS tetrahedron, we show that R13, in addition to
109 axis orientation, is able to infer the consistent current density, helical handedness, curvature
110 radius, and boundaries of flux rope.

111 This paper is organized as follows: the method of R13 is briefly reviewed in Section 2; the
112 overview of studied MFR cases by MMS and the associated multi-point analysis results are
113 offered in Section 3; using R13, the axis orientation, current density, helical handedness,
114 curvature radius of magnetic field lines, and transverse boundaries of MFR are calculated and
115 identified in Section 4; and the conclusion and discussion are finally given in Section 5.
116

2. Review of R13

Rong et al., [2013] presented a single-point method based on the sampled magnetic field data by spacecraft to infer the axis orientation of MFR. This method makes two key assumptions are made in this method: (1) the relative trajectory of spacecraft crossing the MFR is straight; (2) the magnetic field structure of MFR is stable and can be seen as an ideal structure of azimuthal symmetry. The assumptions are usually acceptable, particularly for the innermost part of MFR where the field structure is the least affected by the interaction with ambient plasma. The available data are the relative velocity of spacecraft to cross MFR, **V**, and the sampled magnetic field vector, **B**, by spacecraft. The unit vector of relative velocity and magnetic field are $\hat{\mathbf{v}}$ ($\hat{\mathbf{v}}$ =**V**/|**V**|) and $\hat{\mathbf{b}}$ ($\hat{\mathbf{b}}$=**B**/|**B**|) respectively.

The first step in applying this method is to seek out the innermost location where the spacecraft, along its trajectory, is closest to the center of MFR. In the cross-section of MFR, Figure 1a shows that $\mathbf{v}_\perp$ and $\mathbf{b}_\perp$, the components of $\hat{\mathbf{v}}$ and $\hat{\mathbf{b}}$ perpendicular to the axis orientation respectively, would become parallel or antiparallel at the innermost location, and $\mathbf{v}_\perp \cdot \mathbf{b}_\perp$ would reach the extreme. Hence, by checking the time series of $\hat{\mathbf{v}} \cdot \hat{\mathbf{b}}$, the data point of innermost location could be identified. The identification of the innermost location is a key step in determining the axis orientation, because the axis orientation $\hat{\mathbf{n}}$, the unit field direction at the innermost time $\hat{\mathbf{b}}_{\text{in}}$, and $\hat{\mathbf{v}}$ should be coplanar (see Figure 1b).

The second step is to find the axis orientation $\hat{\mathbf{n}}$ in the plane formed by $\hat{\mathbf{b}}_{\text{in}}$ and $\hat{\mathbf{v}}$. Using the derived $\hat{\mathbf{b}}_{\text{in}}$, one can construct an orthogonal coordinate system $\{\hat{\mathbf{e}}_1, \hat{\mathbf{v}}, \hat{\mathbf{n}}_0\}$ to seek $\hat{\mathbf{n}}$ (see Figure 1b), where

138
$$\hat{\mathbf{e}}_1 = \hat{\mathbf{v}} \times \hat{\mathbf{b}} / |\hat{\mathbf{v}} \times \hat{\mathbf{b}}|$$
$$\hat{\mathbf{n}}_0 = \hat{\mathbf{e}}_1 \times \hat{\mathbf{v}} \quad (1)$$

139 In the plane constituted by $\hat{\mathbf{b}}_{in}$ and $\hat{\mathbf{v}}$, the unsolved axis orientation $\hat{\mathbf{n}}$ deviates from $\hat{\mathbf{n}}_0$ by
140 an angle of ψ. In other words, $\hat{\mathbf{n}}$ is a function of ψ. To constrain ψ, the evaluated impact
141 distance r_0 (the closest distance of MFR's center to spacecraft trajectory) for each data point
142 should be constant along the trajectory. The solved ψ or the optimal $\hat{\mathbf{n}}$ should result in a
143 constant series of r_0. Thus, Rong et al., [2013] constructed a residue error as a function of ψ,

144
$$\sigma^2 = \frac{1}{M}\sum_i^M (r_{0i} - < r_0 >)^2 \quad (2)$$

145 where, M is the number of data points and $< r_0 >= \frac{1}{M}\sum_i^M (r_{0i})$. The axis orientation $\hat{\mathbf{n}}$ can be
146 numerically solved when σ^2 reaches a minimum.

147 Here, to nondimensionalize the residue error, we suggest modifying Eq. (2) as

148
$$\sigma^2 = \frac{1}{M}\sum_i^M \left(1 - \frac{r_{0i}}{\langle r_{0i} \rangle}\right)^2 \quad (3)$$

149

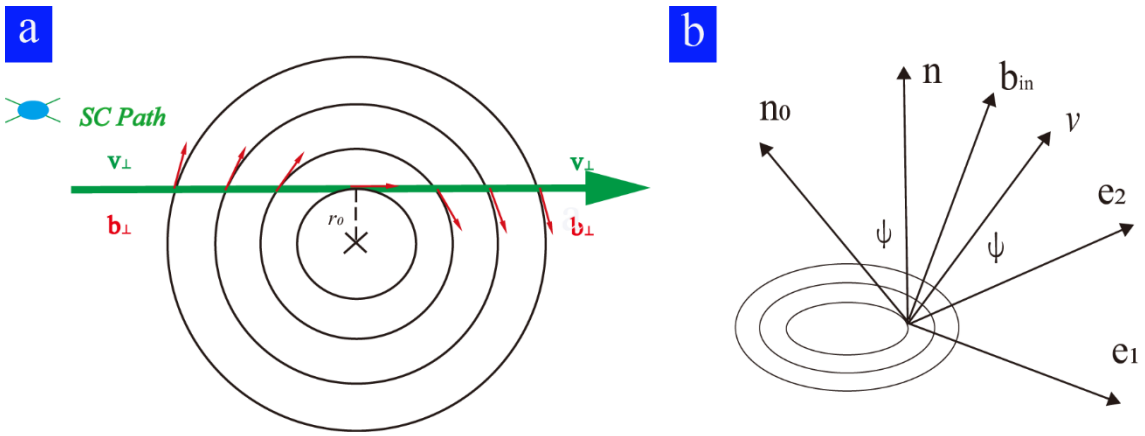

150

151

Figure 1: *Two schematic views of MFR. Panel a shows the variation of unit magnetic field direction along the trajectory of the spacecraft on the cross-section plane. The green arrow denotes the trajectory of the spacecraft, or can be regarded as the direction of* $\mathbf{v}_\perp$. *The red arrows represent the direction of* $\mathbf{b}_\perp$. r_0*, as the impact distance, which is the closest distance to the center of the flux rope. Panel b shows the geometric relationship between* $\{\hat{\mathbf{e}}_1, \hat{\mathbf{v}}, \hat{\mathbf{n}}_0\}$ *and* $\{\hat{\mathbf{e}}_1, \hat{\mathbf{e}}_2, \hat{\mathbf{n}}\}$.

With the optimal $\hat{\mathbf{n}}$ derived from Eq.(3), one can set up an orthogonal coordinate system $\{\hat{\mathbf{e}}_1, \hat{\mathbf{e}}_2, \hat{\mathbf{n}}\}$, and associated cylindrical coordinates $\left\{\hat{\mathbf{r}}, \hat{\boldsymbol{\phi}}, \hat{\mathbf{n}}\right\}$ to describe the intrinsic helical field structure of MFR, where $\hat{\mathbf{e}}_2 = \hat{\mathbf{n}} \times \hat{\mathbf{e}}_1$ (see Figure 1b), $\hat{\mathbf{r}}$ is the unit radial vector from the center of MFR, and $\hat{\boldsymbol{\phi}}$ is the unit azimuthal vector. In the cylindrical coordinates, the axial and azimuthal components of current density can be calculated respectively based on

$$j_n = \mu_0^{-1} r^{-1} \frac{\partial (r B_\phi)}{\partial r}, j_\phi = -\mu_0^{-1} \frac{\partial B_n}{\partial r} \tag{4}$$

where μ_0 is the vacuum permeability coefficient, r is the radial distance to MFR's center, B_n and B_ϕ are the axial and azimuthal components of magnetic field respectively.

In this case, the curvature of magnetic field line of MFR, known as $\boldsymbol{\rho}_\mathbf{c} = (\hat{\mathbf{b}} \cdot \nabla)\hat{\mathbf{b}}$, can be reduced to

$$\boldsymbol{\rho}_c = -\frac{b_\phi^2}{r}\hat{\mathbf{r}} \tag{5}$$

where b_ϕ is the azimuthal component of $\hat{\mathbf{b}}$. Thus, the geometrical field structure of MFR can be also determined readily by cylindrical coordinates.

3 Multi-point analysis of case

In this section, we apply R13 to study the magnetic structure of an MFR case observed by MMS. Comparison with other methods, particularly with multi-point methods, highlights the validity and plausibility of R13. The system utilized here is the Geocentric Solar Ecliptic (GSE) coordinates unless otherwise stated.

3.1 Overview of case

Figure 2 shows an MFR case of ion-scale observed by MMS during 13:04:32-13:04:36 on 16 October 2015. MMS was located at [X=8.33, Y=8.51, Z=-0.7] R_E, around the dayside magnetopause during this period, and the separation scale of the tetrahedron was about 20 km. This case, known as flux transfer events (FTEs) around magnetopause, has been studied by many researchers [Eastwood et al., 2016; Zhao et al., 2016; Akhavan-Tafti et al., 2018].

The detected magnetic field data in Figure 2a shows bipolar signatures (-/+) for both B_x and B_z components accompanied by enhanced magnetic field strength and ion flow of -Vz direction. These typical field signatures of MFR suggest that MMS3 may encounter a southward-moving MFR. The ion and electron number density evidence a slight tendency to decrease towards MFR's center, from ~$14cm^{-3}$ to $5cm^{-3}$, and the plasma beta (the ratio of plasma pressure to magnetic pressure) reaches a minimum around the center of MFR. The signatures of both magnetic field and plasma are consistent with those reported in previous studies of MFR [e.g. Slavin et al., 2003a; Akhavan-Tafti et al., 2018; Sun et al., 2019].

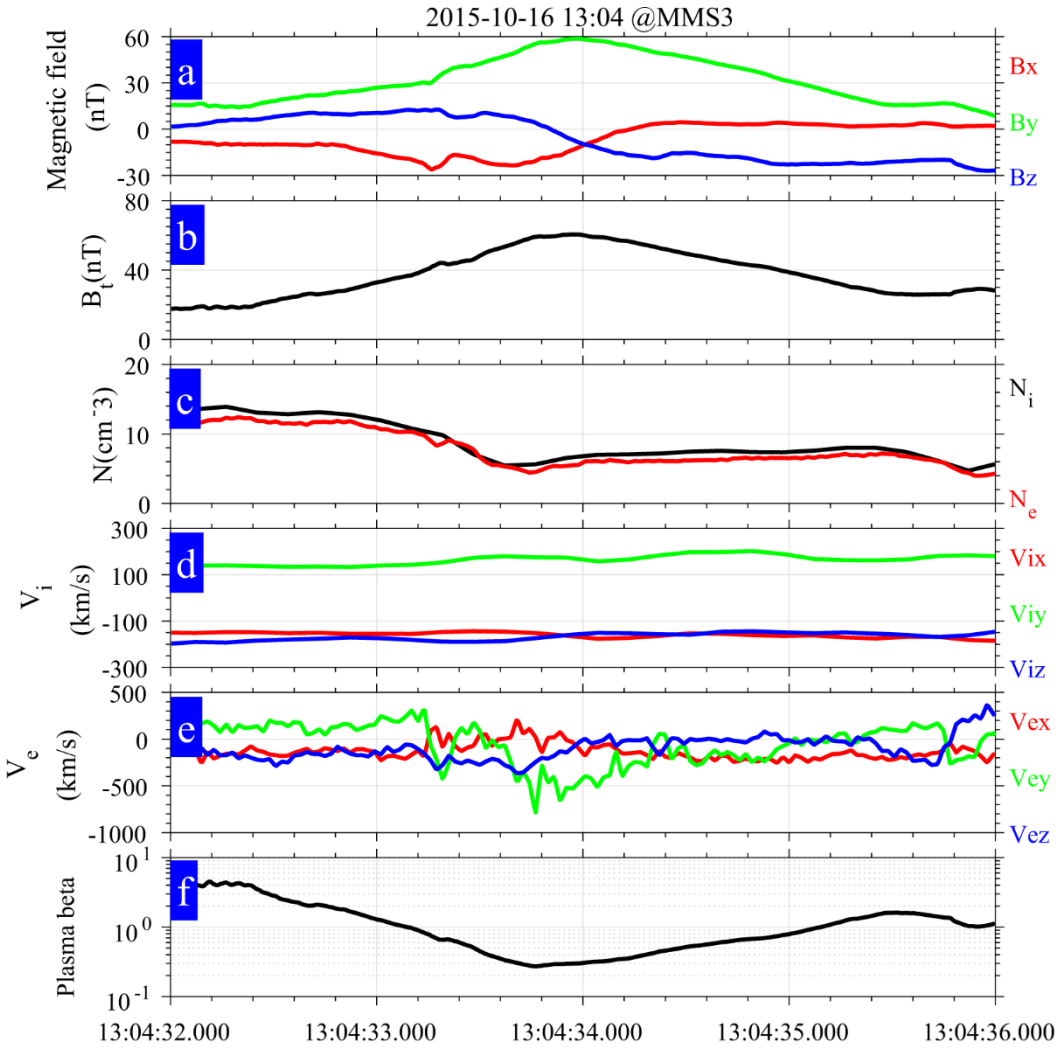

Figure 2: *The flux rope case observed by MMS3 on 16 Oct. 2015. From up to bottom, the panels show the time series of magnetic field components in GSE, the field strength, the number density of ion and electron, the bulk velocity of ions and electrons in GSE, and the value of plasma beta.*

3.2 Multi-Point Analysis

Previous studies suggested that the scale of MFR is about several hundred kilometers [Eastwood et al., 2016; Akhavan-Tafti et al., 2018], which is larger than the scale of MMS tetrahedron (~20 km). Thus, the magnetic field within tetrahedron could be better approximated

by linear-varied field, which favors the application of multi-point analysis methods to examine the geometric structure of a magnetic field, e.g. axis orientation, current density, curvature radius of magnetic field, etc. The parameters of field structure yielded could be treated as a benchmark for checking the validity of R13.

In this subsection, two popular multi-point analysis methods, i.e. MDD (Minimum Directional Derivative) and MRA (Magnetic Rotation Analysis), are used independently to infer the axis orientation.

MDD can determine the dimensionality of magnetic structure and has been successfully applied to analyzing the structure of flux rope [Shi et al., 2005; Shi et al., 2019; Sun et al., 2019]. The key step is to decompose the symmetrical matrix $(\nabla\mathbf{B})(\nabla\mathbf{B})^{\mathrm{T}}$, where $\nabla\mathbf{B}$ is the gradient tensor of magnetic field. Three eigenvalues $(\lambda_{\max},\lambda_{\mathrm{int}},\lambda_{\min})$ and the corresponding eigenvectors $(\hat{\mathbf{n}}_{\max},\hat{\mathbf{n}}_{\mathrm{int}},\hat{\mathbf{n}}_{\min})$ can be obtained by decomposing $(\nabla\mathbf{B})(\nabla\mathbf{B})^{\mathrm{T}}$. The dimensionality of magnetic structure can be indicated by the three eigenvalues. If magnetic structure is 1-D, we would have $\sqrt{\lambda_{\max}} \gg \sqrt{\lambda_{\mathrm{int}}} \cong \sqrt{\lambda_{\min}}$, it would be $\sqrt{\lambda_{\max}} \cong \sqrt{\lambda_{\mathrm{int}}} \gg \sqrt{\lambda_{\min}}$ if it is 2-D.

Applying MDD to this case (see Figure 3a), we find $\sqrt{\lambda_{\max}}$ ~0.35, $\sqrt{\lambda_{\mathrm{int}}}$ ~0.25, and $\sqrt{\lambda_{\min}}$ ~0.03 around the peak of magnetic field. Thus, the MFR is a 2-D structure, and the axis orientation is along $\hat{\mathbf{n}}_{\min}$ [Shi et al., 2005; Shi et al., 2019]. We select an appropriate time interval when $\hat{\mathbf{n}}_{\min}$ is stable around the peak of magnetic field (see the shaded interval '13:04:33.950-13:04:34.350' in Figure 3b). The mean of $\hat{\mathbf{n}}_{\min}$ within this interval demonstrates that the axis orientation is (-0.2618, 0.9416, -0.2119).

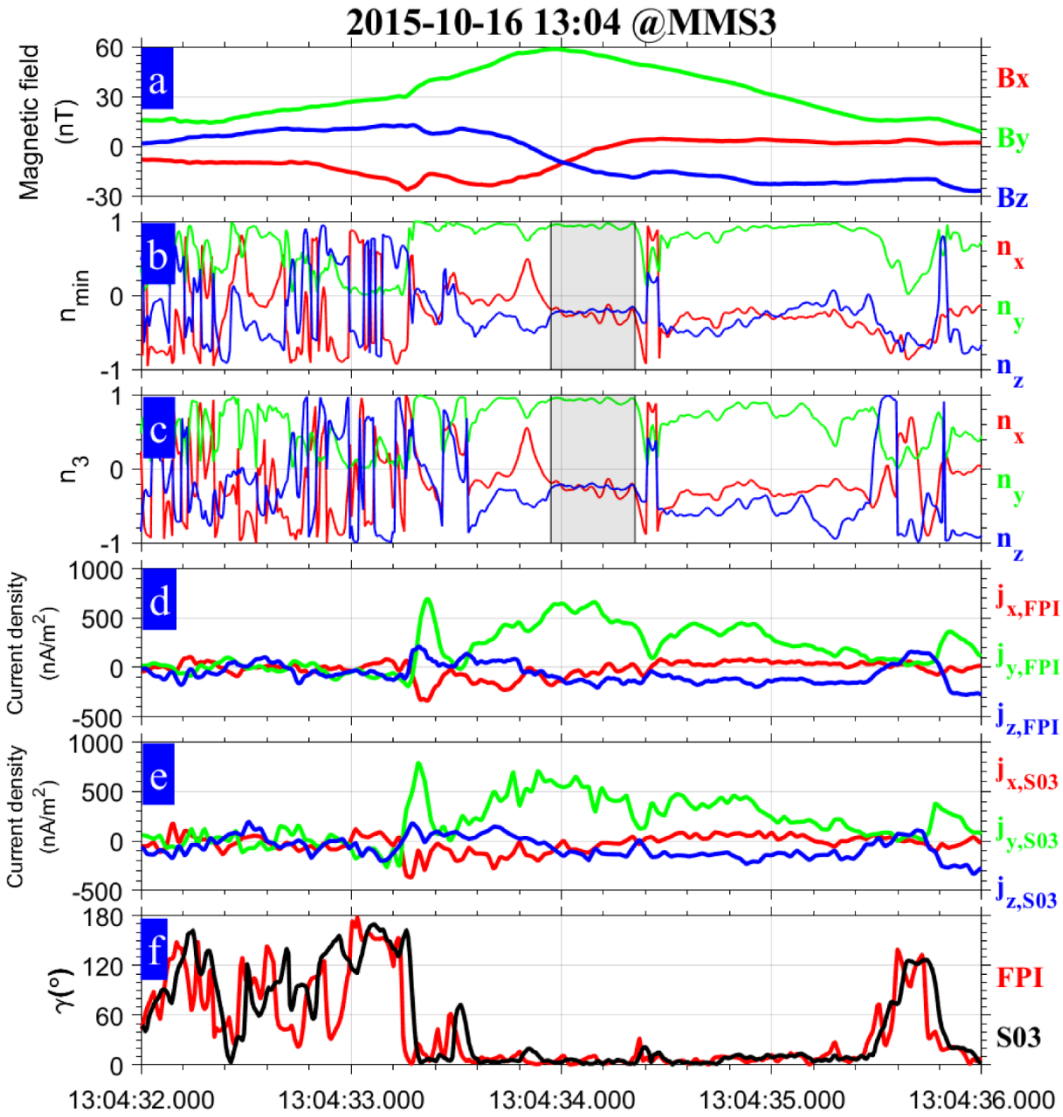

***Figure 3**: Multi-point analysis of a flux rope. From top to bottom, panels show: (a) magnetic field; (b) the eigenvector corresponding to λ_{min} in MDD; (c) the eigenvector corresponding to μ_3 in MRA; (d) the current density derived by multi-point analysis of magnetic field; (e) current density derived by plasma moments from FPI of MMS3; (f) the angle between current density and the direction of magnetic field.*

In contrast to MDD, MRA is performed to analyze the spatial rotation rates of magnetic field direction by decomposing the magnetic rotation tensor $(\nabla\hat{\mathbf{b}})(\nabla\hat{\mathbf{b}})^{\mathrm{T}}$ [Shen et al., 2007]. The decomposition of this tensor leads to three eigenvalues (μ_1, μ_2, μ_3) and three eigenvectors $(\hat{\mathbf{n}}_1, \hat{\mathbf{n}}_2, \hat{\mathbf{n}}_3)$. $\hat{\mathbf{n}}_1$, $\hat{\mathbf{n}}_2$, and $\hat{\mathbf{n}}_3$ represent the fastest, moderate, and slowest directions, respectively, along which the direction of magnetic field varies. Thus, $\hat{\mathbf{n}}_3$ is usually seen as the axis orientation of MFR when it was surveyed [Shen et al., 2007; Yang et al., 2014]. The time series of calculated $\hat{\mathbf{n}}_3$ is displayed in Figure 3c. With the same shaded interval in Figure 3b, the average axis orientation derived by MRA is (-0.2679, 0.9338, -0.2373), which is nearly equal to that obtained by MDD. The inferred axis orientations from MDD and MRA are tabulated in Table 1.

According to $\mathbf{j} = \mu_0^{-1}\nabla \times \mathbf{B}$, the current density can be also solved based on a multi-point analysis that uses Taylor expansion by Shen et al., [2003] (it is referred to as S03). The calculated current density is shown in Figure 3d. Alternatively, with plasma moments measured by FPI onboard MMS3, Figure 3e shows the current density calculated by $\mathbf{j} = \mathbf{n_e e}(\mathbf{V_i} - \mathbf{V_e})$, where $\mathbf{n_e}$ is the number density of electron, while $\mathbf{V_i}$ and $\mathbf{V_e}$ are the bulk velocity of protons and electrons respectively. Apparently, the two methods to calculate the current density shows much agreement, demonstrating that measurement of plasma moments by FPI can be employed to calculate the current density, and that the electron could be the main current carrier of MFR (not shown here).

The angle between current density and magnetic field, denoted as γ, is nearly equal to 0° in the center and trail of MFR (see Figure 3f), which indicates that the current density is basically

field-aligned, and suggests that the field structures at MFR's center and trail are close to the force-free field with a right-hand helical handedness [Eastwood et al., 2016].

4. Application of R13

4.1 Axis Orientation

We now perform R13 to analyze the field structure of this flux rope. Without loss of generality, we arbitrarily choose the data provided by MMS3 for our analysis.

Following the procedures of Rong et al., [2013], we identify the innermost time first by checking the time series of $\hat{\mathbf{v}} \cdot \hat{\mathbf{b}}$. With the assumption of crossing a quasi-stationary magnetic structure, the velocity of MFR can be seen as $\mathbf{V}_{\mathrm{HT}}$, the velocity of DeHoffmann-Teller (HT) frame [Khrabrov and Sonnerup, 1998]. Thus, with HT analysis within interval 13:04:32-13:04:36, the relative velocity of spacecraft to MFR is calculated as $\mathbf{V} = -\mathbf{V}_{\mathrm{HT}}$ = (167.88, -208.83, 165.94) km/s. The correlation coefficient ~0.998 between $-\mathbf{V}_{\mathrm{HT}} \times \mathbf{B}$ and $-\mathbf{V} \times \mathbf{B}$ ($\mathbf{V}$ is the bulk ion velocity from FPI) guarantees the reliability of HT analysis. As a result, the unit vector of $\hat{\mathbf{v}}$ is derived as $\hat{\mathbf{v}} = \dfrac{\mathbf{V}}{|\mathbf{V}|}$ = (0.5327, -0.6626, 0.5265).

Figure 4a shows the time series of $\hat{\mathbf{v}} \cdot \hat{\mathbf{b}}$. Clearly, the product of $\hat{\mathbf{v}} \cdot \hat{\mathbf{b}}$ reaches a minimum around the peak of field strength (Figure 4b). Thus, corresponding to the minimum of $\hat{\mathbf{v}} \cdot \hat{\mathbf{b}}$, the time when the spacecraft is located at the innermost part or is closest to the MFR's center can be identified at 13:04:33.982 (see the red dashed lines in Figure 4a and Figure 4b). Accordingly, having identified the innermost time, the inferred $\hat{\mathbf{e}}_1$ is (-0.7295, -0.0442, 0.6825), $\hat{\mathbf{n}}_0$ is (0.4290, 0.7477, 0.5069), and the local coordinate system $\{\hat{\mathbf{e}}_1, \hat{\mathbf{v}}, \hat{\mathbf{n}}_0\}$ can be constructed via Eq. (1).

We choose a short interval centered at the innermost time with 20 sampled magnetic field vectors to infer the axis orientation (a longer interval may contain the samples nearby the boundary where field structures are significantly distorted). It should be noted that, as suggested by Rong et al. [2013], the sampled data point at the innermost time has been excluded to avoid the ill-calculation. By numerical calculation, we find that the residue error σ, defined in Eq. (3), would reach a minimum ($\sigma_{min}=0.015$) when the angle between $\hat{\mathbf{n}}$ and $\hat{\mathbf{n}}_0$, equals either 126.18° or 306.18° (Figure 4c), which results in a pair of anti-parallel axis-orientations in principle. Following Rong et al., [2013], we choose the one pointing roughly along $\hat{\mathbf{b}}_{in}$ as the final axis orientation. As a result, the axis orientation $\hat{\mathbf{n}}$ is derived as (-0.1767, 0.9762, -0.1257), and $\hat{\mathbf{e}}_2$ is estimated as (0.6607, 0.2123, 0.7200). In other words, projected along the derived $\hat{\mathbf{n}}$, the orientations of the 20 magnetic vectors in trajectory can be fitted best with a circular-like field structure. We find the mean impact distance of those 20 data points is about ~3.2 km (see Figure 4d), which indicates that, in this case, MMS3 was almost crossing MFR's center.

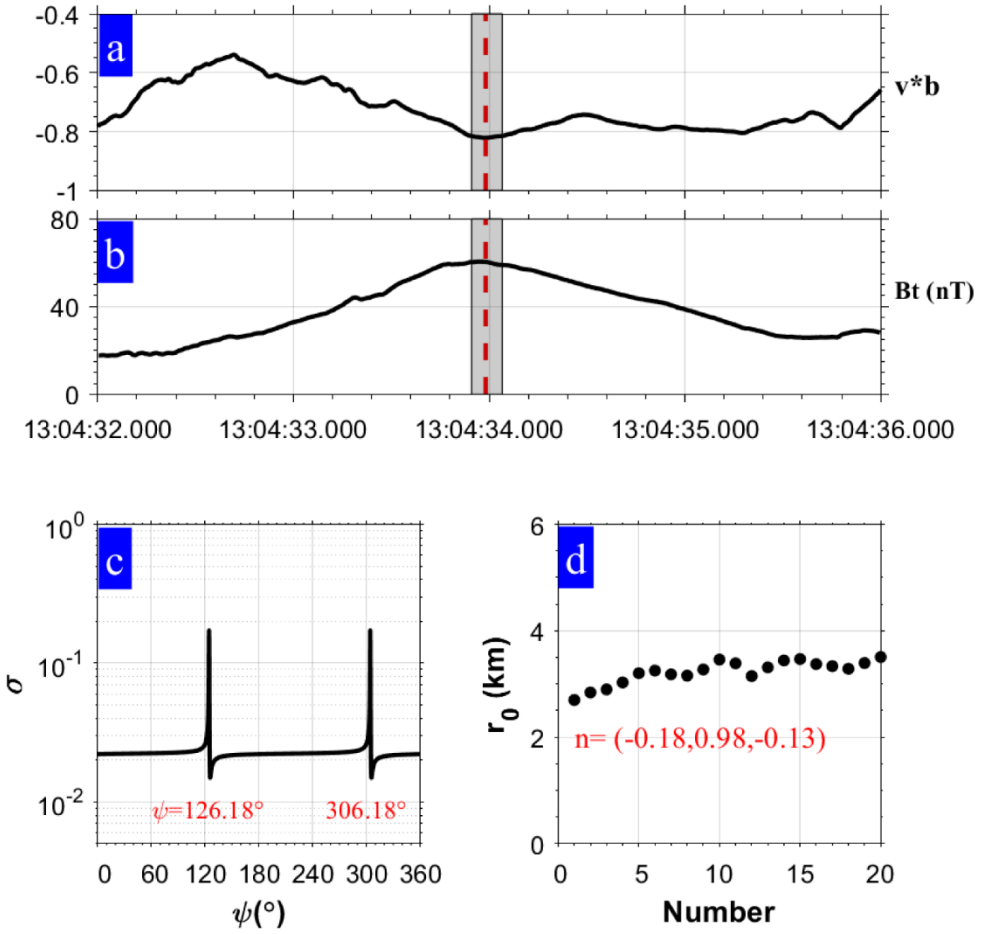

Figure 4*: Analysis of a flux rope based on the single-point method proposed by Rong et al., [2013]. Panel a and panel b show the time series of* $\hat{\mathbf{v}}\cdot\hat{\mathbf{b}}$ *and the magnetic field strength respectively. The red dashed lines mark the time when* $\hat{\mathbf{v}}\cdot\hat{\mathbf{b}}$ *reaches a minimum. Panel c shows the variation of* σ *against* ψ*. Panel d displays the evaluated impact distances for the 20 data points of magnetic vectors.*

Since $\hat{\mathbf{e}}_1$, $\hat{\mathbf{e}}_2$ and $\hat{\mathbf{n}}$ are inferred, the orthogonal coordinate system $\{\hat{\mathbf{e}}_1,\hat{\mathbf{e}}_2,\hat{\mathbf{n}}\}$ is set up to describe the intrinsic helical field structure of MFR. In this coordinate, Figure 5a shows the projection of sampled $\mathbf{b}$ (within the shaded interval) in the cross-section. Obviously, the

296 loop-like pattern of the projected field (also see Figure 5b) is consistent with the field-aligned
297 current density near MFR center (see Figure 3c), which demonstrates the validity of R13.
298

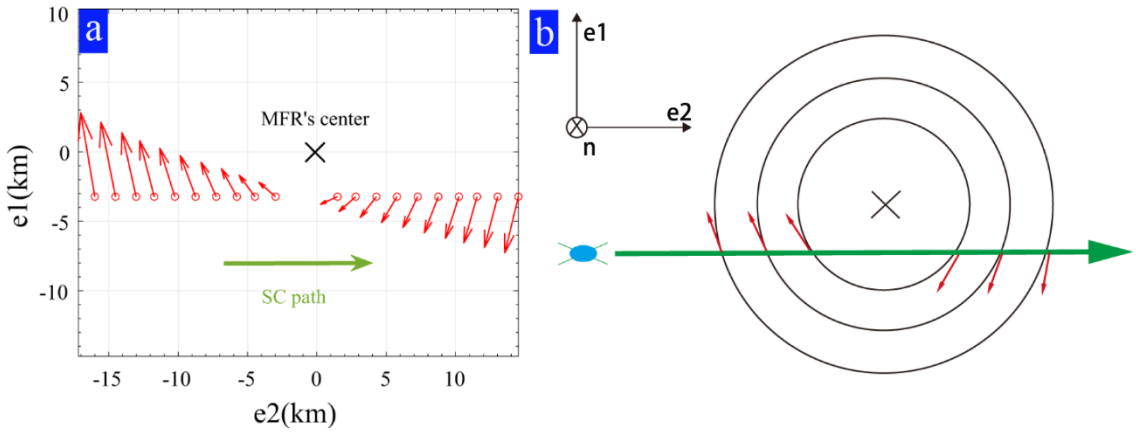

299

300 ***Figure 5****: (a) The projection of unit field vectors of sampled data points on the* $\hat{\mathbf{e}}_1 - \hat{\mathbf{e}}_2$ *plane.*
301 *The red arrows represent the orientations of* $\mathbf{b}_\perp$*, and the green arrow represents the relative*
302 *moving direction of the spacecraft crossing the MFR. The origin, marked as "×", represents the*
303 *MFR's center. (b) A sketched diagram of the spacecraft crossing the MFR.*
304

305 Repeating the same procedures as being conducted above, the axis orientations of this MFR
306 based on the measurements of MMS1, MMS2, MMS4 are also inferred separately. The yielded
307 results are tabulated in Table 1. As a comparison, the axis orientations by means of MDD and
308 MRA, and fitting of force-free model [Eastwood et al., 2016], and a minimum variance analysis
309 on gradient of magnetic pressure [Zhao et al., 2016] are also tabulated in Table1. In contrast to
310 the single-point fitting method used by Eastwood et al. [2016], it seems the axis orientation
311 inferred by R13 is closer to the axis orientation estimated by multi-point methods, i.e. MDD,
312 MRA, and the analysis of magnetic pressure gradient by Zhao et al. [2016].
313

Table 1: The inferred axis-orientations by different methods.

SC[a]	$\hat{\mathbf{e}}_1$	$\hat{\mathbf{e}}_2$	$\hat{\mathbf{n}}$	Method[b]
MMS1	[-0.77, -0.10, 0.63]	[0.60, 0.22, 0.77]	[-0.21, 0.97, -0.11]	R13
MMS2	[-0.72, -0.02, 0.69]	[0.68, 0.17, 0.71]	[-0.14, 0.98, -0.11]	R13
MMS3	[-0.73, -0.04, 0.68]	[0.66, 0.21, 0.72]	[-0.18, 0.97, -0.13]	R13
MMS4	[-0.73, -0.05, 0.68]	[0.64, 0.30, 0.71]	[-0.24, 0.95, -0.19]	R13
All			[-0.24, 0.95, -0.22]	MDD
All			[-0.25, 0.94, -0.23]	MRA
MMS3			[-0.01, 0.99, -0.15]	E16
All			[-0.26, 0.90, -0.36]	Z16

[a] *SC represents the spacecraft whose data is used.*

[b] *R13, E16, and Z16 represents, respectively, the single-point method presented by Rong et al., [2013], the fitting of force-free model by Eastwood et al., [2016], and the minimum variance analysis on the gradient of magnetic pressure by Zhao et al., [2016].*

4.2 Current density and Curvature radius

With the derived coordinate system $\{\hat{\mathbf{e}}_1, \hat{\mathbf{e}}_2, \hat{\mathbf{n}}\}$ for each spacecraft, we can examine the current density and the curvature radius of magnetic field for associated cylindrical coordinates $\{\hat{\mathbf{r}}, \hat{\boldsymbol{\phi}}, \hat{\mathbf{n}}\}$ based on Eq. (4) and Eq. (5) respectively. The time series of calculated axial component of current density, j_n, and the azimuthal component of current density, j_ϕ, for MMS1, MMS2, MMS3, and MMS4 are shown in Figure 6a-6d and Figure 6e-6h, respectively. The angle between current density and magnetic field, denoted as γ, is shown in Figure 6i-6l for the four spacecraft.

In comparison to the current density calculated by $\mathbf{j} = n_e e(\mathbf{V}_\mathrm{i} - \mathbf{V}_\mathrm{e})$ (black line) and $\mathbf{j} = \mu_0^{-1} \nabla \times \mathbf{B}$ by S03 from (blue line), we find that the current density calculated by R13 for each of the four spacecraft are consistent with that derived from the plasma moments and the curl of magnetic field. From this latter current density, we notice a significant field-aligned current in the MFR center and a filament peak of current ahead of it, suggesting that the magnetic field is

nearly force-free around the center but non-force-free in the outer or the draping region [Zhao et al., 2016]. The consistent pattern of current density demonstrates that the method of R13 can recover the distribution of current density of MFR (red line) by means of a one-point analysis.

The curvature radius of magnetic field is calculated separately for each of the four spacecraft via Eq. (5), as shown in Figure 6m-6p. For comparison, the curvature radius calculated by S03 is displayed. It is clear that the curvature radius from S03 is larger in MFR's center (~0.25 R_E) than in the outer region (~0.05R_E), which implies that magnetic field lines become straighter in the MFR's center. This is consistent with previous studies [e.g., Slavin et al., 2003; Shen et al., 2007; Yang et al., 2014]. It is interesting to note that R13 obtains the similar pattern of curvature radius variation, but slightly overestimates the curvature radius. Because R13 ignores axial and azimuthal components and only estimates the radial component of curvature, the real curvature is underestimated and curvature radius is overestimated. The discrepancy demonstrates that the actual field structure in the inner core of MFR cannot be an ideal structure of azimuthal symmetry.

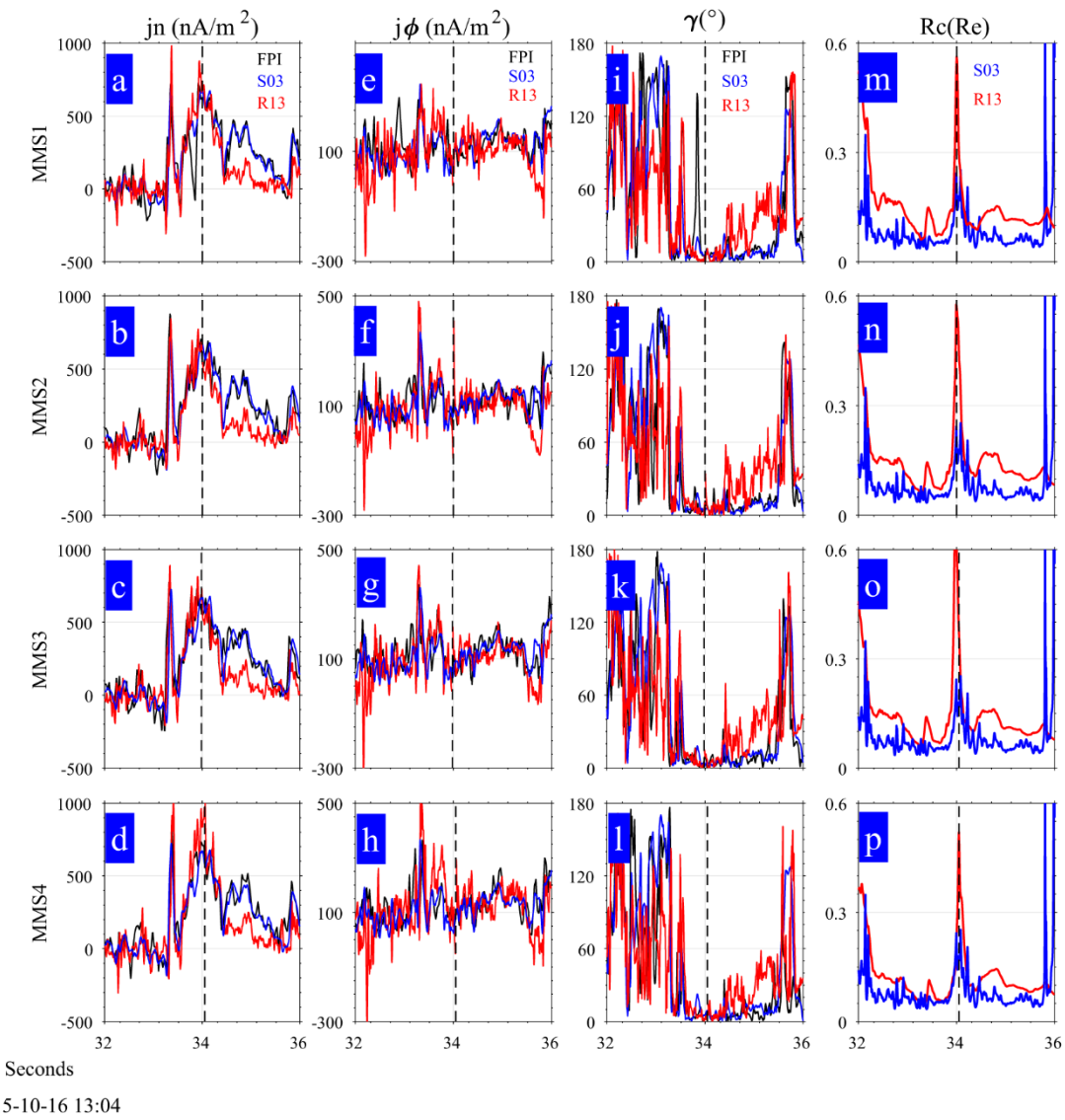

***Figure 6**: The current density and curvature radius of MFR. The inferred axial components (j_n) of current density for four spacecraft are shown in panels a-d, the azimuthal components (j_ϕ) of current density are shown in panels e-h, and the angles between current density and local magnetic field direction are shown in panels i-l. The inferred curvature radiuses of magnetic field are shown in panels m-p. In these panels, the red and black lines represent the single-point results by R13 and plasma moment of FPI respectively. The blue lines represent the results of multi-point analysis by S03, which is the same for all panels in each column. The black dashed lines in all panels denote the time when the spacecraft is closest to the center of MFR.*

4.3 Boundary or Size

With the derived axis orientation by R13, we could further study the helical field structure of MFR, and identify its boundaries or transverse size.

In the cross-section near the center of MFR (shown in Figure 7a), the projected magnetic field would be close to a circular configuration, and the displacement vector ($\mathbf{r}$, cyan lines) should be nearly perpendicular to the magnetic field vector ($\mathbf{b}_\perp$, red arrows). The angle $\alpha_{r,b_\perp}$, defined as $\alpha_{r,b_\perp} = a\cos(|\mathbf{r}\cdot\mathbf{b}_\perp|/\mathbf{r}\cdot\mathbf{b}_\perp)$, is presumably close to $90°$ around the center of MFR. In contrast, in the outer part or boundary, $\alpha_{r,b_\perp}$ would deviate from $90°$ due to the distorted field structure induced by interaction with ambient plasma. Thus, the boundaries of MFR could be identified by checking the time series of $\alpha_{r,b_\perp}$. The time series of $\alpha_{r,b_\perp}$ recorded by MMS3 is shown in Figure 7b. As expected, during the passage of MFR by spacecraft, $\alpha_{r,b_\perp}$ increases when the spacecraft moves towards MFR's center, stay about $90°$ when around the inner part, and finally decreases as it moves away from MFR.

Further, one can define a helical angle as $\theta = acos\left(\frac{B_\phi}{B_t}\right)$, where $B_\phi = |\mathbf{B} - (\mathbf{B}\cdot\hat{\mathbf{n}})\hat{\mathbf{n}}|$, to study the helical geometry of MFR's field. Since the magnetic field in MFR's center is nearly parallel to the axis orientation, one would expect an increased helical angle when the distance to MFR's center is decreased. Figure 7c shows the calculated helical angle by R13 during the whole passage of MFR. For comparison, according to the axis orientation inferred from MRA, the helical angle from multi-point analysis is also displayed. The two methods yield an almost coincident time series of helical angle, suggesting the validity of the derived axis orientation by R13. In line with our expectations, we find the calculated helical angle increases as the

spacecraft approaches the innermost location, and decreases as it moves away from MFR. The maximum helical angle of nearly 90° demonstrates that the field lines around the innermost part are almost parallel to the axis orientation.

Therefore, considering the variation of $\alpha_{r,b_\perp}$, the helical angle, and the axial component of magnetic field and field strength (Figure 7d), we suggest that the inbound and outbound crossing time of MFR boundaries should be 13:04:32.708 and 13:04:35.404, respectively. Thus, the interval of crossing the MFR is about 2.7 s (see the shaded interval in Figure 7b-7f). It is worthwhile to note that, with our identification of the boundaries, the frontal region or outer draping region with non-force-free field could be reasonably included within MFR (Figure 7e).

With the knowledge of axis orientation and the relative velocity of spacecraft ($\mathbf{V} = -\mathbf{V}_{HT}$), the transverse speed of crossing spacecraft is $|\mathbf{V}_\perp| = |\mathbf{V} - (\mathbf{V}\cdot\hat{\mathbf{n}})\hat{\mathbf{n}}|$=186 km/s; thus the diameter (radius) of MFR is about 502 km (251 km). Interestingly, multi-point analysis by S03 demonstrated that the curvature radius inside MFR is about 0.05 R_E, or 319 km (see Figure 6m-6p), which is comparable to the radius of MFR we estimated. In contrast, with the fit of force-free model, the radius of MFR estimated previously by Eastwood et al. [2016] and Akhavan-Tafti et al. [2018] is about 400~500 km, about twice of our estimation.

In the innermost part of this MFR, which has a low beta (~0.25) and a dominated field-aligned current (see Figure 2f and Figure 7e), the innermost field basically satisfies the force-free field [Lepping et al., 1990; Yang et al., 2014], $\nabla\times\mathbf{B}=\mu_0\mathbf{j}=\alpha\mathbf{B}$. The calculated force-free factor α ($\alpha=\mu_0 j_t / B_t$) demonstrates that α is nearly constant (~0.013 km^{-1}) in the innermost of MFR, suggesting a linearly force-free field (Figure 7f).

Repeating the same procedures, the radius of MFR based on the measurements of MMS1, MMS2, MMS4 are also inferred separately. The results yielded are tabulated in Table 2.

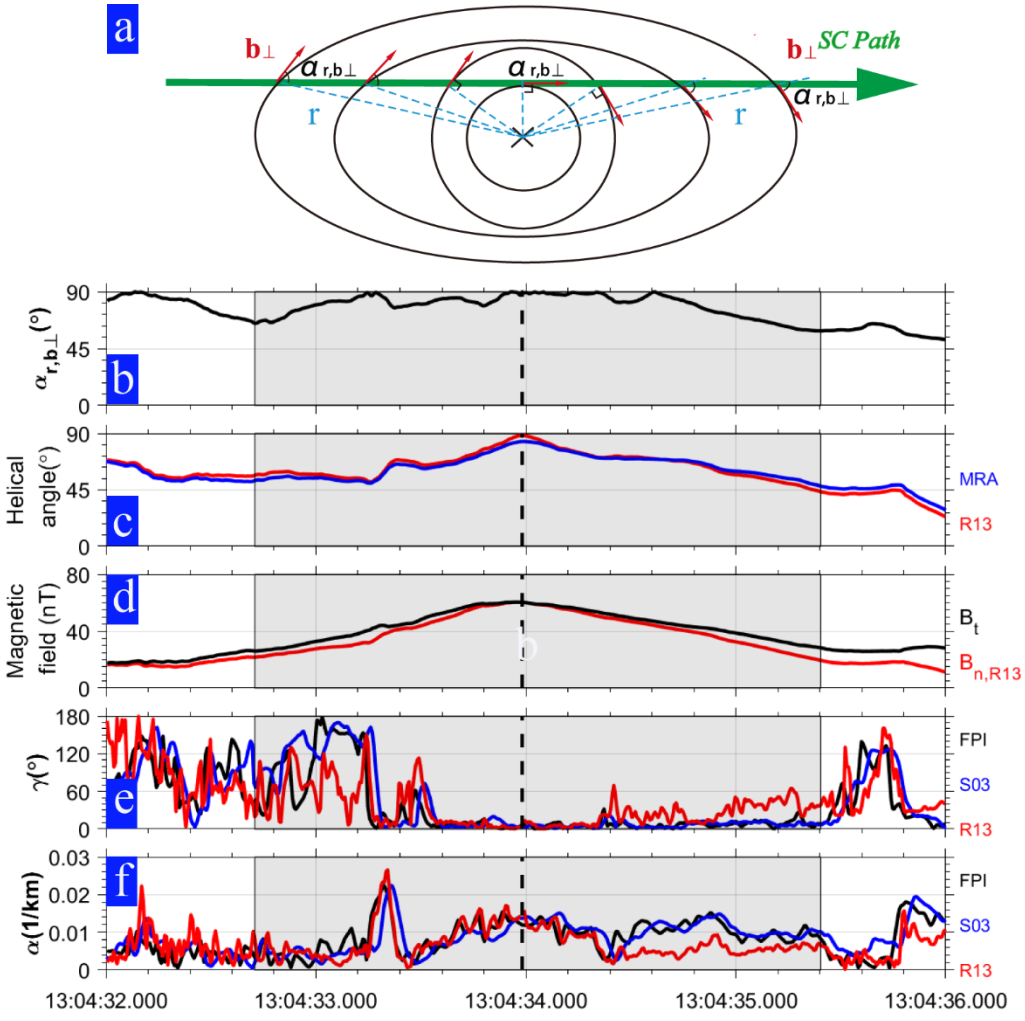

***Figure 7**: (a) A sketched diagram of flux rope; (b) the angle between the displacement vector and the direction of magnetic field (see definition in the text); (c) the helical angle; (d) the strength of magnetic field and the axial component of magnetic field derived from R13; (e) the angle between current density and orientation of magnetic field; (f) the force-free factor α. The black shaded interval represents the period of crossing the flux rope. The black dashed line denotes the time when the spacecraft is closest to the center of MFR.*

Table 2: The inferred radius of MFR.

SC[a]	Interval[b]	$V_{\perp}(km/s)$	R(km)[c]	Method[d]
MMS1	13:04:32.808-13:04:35:590	186.42	259	R13
MMS2	13:04:32.736-13:04:35:572	199.95	284	R13
MMS3	13:04:32.708-13:04:35:404	186.06	251	R13
MMS4	13:04:32.784-13:04:35.409	155.58	204	R13
MMS3	~	~	550	E16
~	~	~	431	A18

[a] *SC represents the spacecraft whose data is used. The symbol "~" means that the related information is unclear.*

[b]*The duration of crossing MFR based on the variation of* $\alpha_{r,b_{\perp}}$.

[c]*The radius of MFR.*

[d]*The method applied in analyzing MFR. R13 and E16 are the same as defined in Table1. A18 represents the results based on the fit of force-free model by Akhavan-Tafti et al., [2018].*

Using the inferred axis orientation and the transverse size of MFR based on the measurements of MMS3, we project the field vectors recorded by four spacecraft on the cross-section in Figure 8. The projected magnetic field near the MFR center is circular-like or close to the structure of azimuthal symmetry (see Figure 8b), but is distorted or deviates from the circular-like shape near the boundaries.

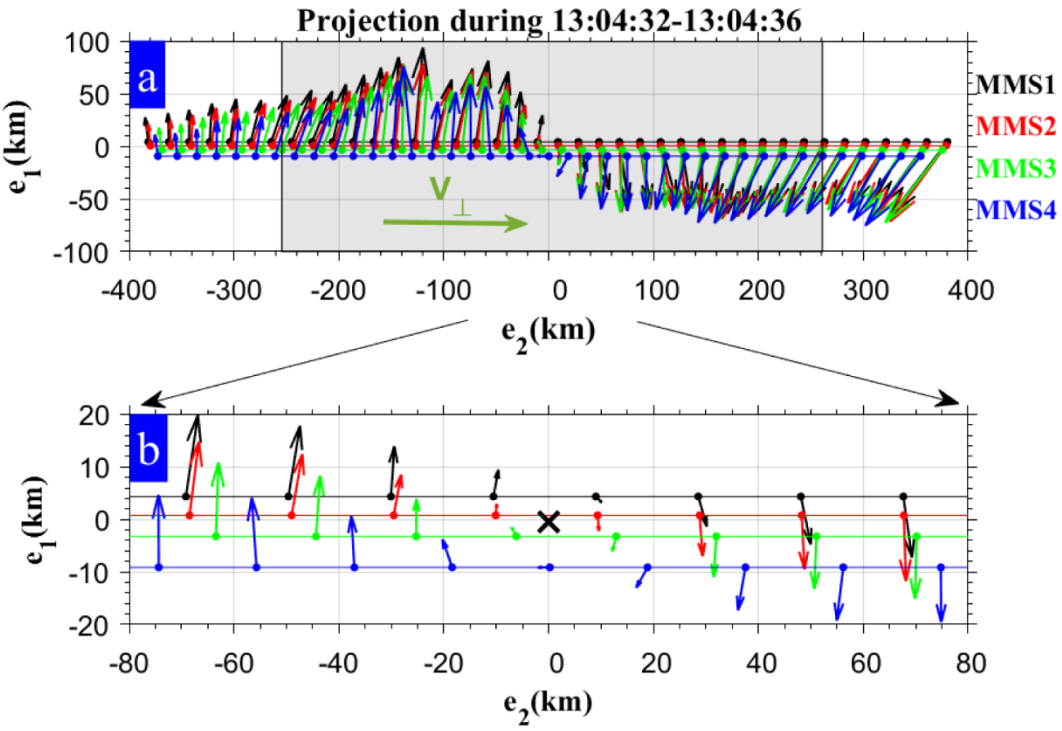

***Figure 8**: The projection of* $\mathbf{b}_\perp$ *on the cross-section of flux rope. The resampled field vectors with a cadence of 0.1s as recorded by MMS1, MMS2, MMS3, MMS4 are labeled in black, red, green, and blue, respectively. The inferred size of MFR is shaded. Panel b zooms in on the projection of magnetic field vectors near the center of MFR.*

4 Conclusion and Discussion

In this paper, by applying R13 to a magnetic flux rope observed by MMS tetrahedron in Earth's magnetopause, we analyze the magnetic field structure of magnetic flux rope. The parameters, including the axis orientation, the current density, the curvature radius of magnetic field, and the transverse size, are estimated by R13. With the estimated parameters, we conclude that: (1) the axis of MFR is basically orientated along the +Y-axis of GSE; (2) the field-aligned current is dominant in the interior of MFR where magnetic field is nearly force-free, and a filament peak of current is present in the leading part of MFR; (3) the helical handedness of

435 MFR is right-handed; (4) the curvature radius of magnetic field is larger in the MFR's center
436 than in the outer region ; (5) MFR's radius is about 250 km, suggesting the ion scale of MFR's
437 size.

438 The comparison with multi-point analysis methods demonstrates that R13 is reliable and
439 applicable. Therefore, the R13 can be applied widely to the "big dataset" accumulated by the
440 single-point spacecraft missions in history, e.g. Geotail, and to the planetary missions, e.g.
441 MAVEN [Jakosky et al., 2015], to study the geometry of flux rope and explore its origin,
442 evolution, and roles in the space environment.

443 We have to note that the key assumption of R13 is azimuthal symmetry of projected field
444 lines near the core of MFR. The assumption is more relaxed than that of the force-free model
445 which is employed to fit MFR in many previous studies [e.g. Burlaga, 1988; Lepping et al., 1990;
446 Slavin et al., 2003b]. However, the real field structure in the core of MFR absolutely cannot have
447 an ideal azimuthal symmetry as demonstrated by the non-zero minimum σ (Figure 4c) and the
448 overestimated curvature radius in MFR's center (Figure 6m-6p). Thus, the yielded parameters by
449 R13 must always be interpreted with caution.

450

451 **Acknowledgments**

452 The magnetic field data and plasma data of MMS used in this paper are available from the
453 MMS Science Data Center at http://lasp.colorado.edu/mms/sdc/. The authors are grateful to the
454 entire MMS team for providing the data. This work is supported by the Strategic Priority
455 Research Program of Chinese Academy of Sciences (Grant No. XDA17010201), the Key
456 Research Program of the Institute of Geology & Geophysics, CAS, Grant No. IGGCAS- 201904,
457 the National Natural Science Foundation of China (grants 41922031，41774188， 41874190,

458 41874176, and 41621063) and NASA MMS Guest Investigator Grant 80NSSC18K1363. We
459 thank Nanqiao Du, Zhen Shi, Xinzou Li, Di Liu and Fang Qian for providing helpful
460 suggestions.

461

462 **References**

463 Akhavan-Tafti, M., Slavin, J. A., Le, G., Eastwood, J. P., Strangeway, R. J., Russell, C. T., …
464 Burch, J. L. (2018). MMS Examination of FTEs at the Earth's Subsolar Magnetopause.
465 *Journal of Geophysical Research: Space Physics, 123*(2), 1224–1241.
466 https://doi.org/10.1002/2017ja024681.
467 Burch, J. L., Moore, T. E., Torbert, R. B., & Giles, B. L. (2015). Magnetospheric Multiscale
468 Overview and Science Objectives. *Space Science Reviews, 199*(1–4), 5–21.
469 https://doi.org/10.1007/s11214-015-0164-9.
470 Burlaga, L. F. (1988). Magnetic clouds and force-free fields with constant alpha. *Journal of*
471 *Geophysical Research, 93*(A7), 7217. https://doi.org/10.1029/ja093ia07p07217.
472 DiBraccio, G. A., Slavin, J. A., Imber, S. M., Gershman, D. J., Raines, J. M., Jackman, C. M., …
473 Solomon, S. C. (2015). MESSENGER observations of flux ropes in Mercury's magnetotail.
474 *Planetary and Space Science, 115*, 77–89. https://doi.org/10.1016/j.pss.2014.12.016.
475 Eastwood, J. P., Phan, T. D., Cassak, P. A., Gershman, D. J., Haggerty, C., Malakit, K., … Wang,
476 S. (2016). Ion-scale secondary flux ropes generated by magnetopause reconnection as
477 resolved by MMS. *Geophysical Research Letters, 43*(10), 4716–4724.
478 https://doi.org/10.1002/2016gl068747.
479 Elphic, R. C., & Russell, C. T. (1983). Magnetic flux ropes in the Venus ionosphere:
480 Observations and models. *Journal of Geophysical Research, 88*(A1), 58.
481 https://doi.org/10.1029/ja088ia01p00058.
482 Escoubet, C. P., Fehringer, M., & Goldstein, M. (2001). *Introduction* The Cluster mission.
483 *Annales Geophysicae, 19*(10/12), 1197–1200. https://doi.org/10.5194/angeo-19-1197-2001.
484 Hara, T., Harada, Y., Mitchell, D. L., DiBraccio, G. A., Espley, J. R., Brain, D. A., … Jakosky,
485 B. M. (2017). On the origins of magnetic flux ropes in near-Mars magnetotail current sheets.
486 *Geophysical Research Letters, 44*(15), 7653–7662. https://doi.org/10.1002/2017gl073754.
487 Hau, L.-N., & Sonnerup, B. U. Ö. (1999). Two-dimensional coherent structures in the
488 magnetopause: Recovery of static equilibria from single-spacecraft data. *Journal of*
489 *Geophysical Research: Space Physics, 104*(A4), 6899–6917.
490 https://doi.org/10.1029/1999ja900002.
491 Hones, E. W., Jr. (1977). Substorm processes in the magnetotail: Comments on "On hot tenuous
492 plasmas, fireballs, and boundary layers in the Earth"s magnetotail' by L. A. Frank, K. L.
493 Ackerson, and R. P. Lepping. *Journal of Geophysical Research, 82*(35), 5633–5640.
494 https://doi.org/10.1029/ja082i035p05633.
495 Hu, Q., & Sonnerup, B. U. Ö. (2002). Reconstruction of magnetic clouds in the solar wind:
496 Orientations and configurations. *Journal of Geophysical Research, 107*(A7), 1142.
497 https://doi.org/10.1029/2001JA000293.

Jakosky, B. M., Lin, R. P., Grebowsky, J. M., Luhmann, J. G., Mitchell, D. F., Beutelschies, G., Priser, T., Acuna, M., Andersson, L., Baird, D., Baker, D., Bartlett, R., Benna, M., Bougher, S., Brain, D., Carson, D., Cauffman, S., Chamberlin, P., Chaufray, J.-Y., … Zurek, R. (2015). The Mars Atmosphere and Volatile Evolution (MAVEN) Mission. *Space Science Reviews, 195*(1–4), 3–48. https://doi.org/10.1007/s11214-015-0139-x.

Khrabrov, A. V., and B. U. O. Sonnerup (1998), DeHoffmann-Teller analysis, in Analysis Methods for Multi-Spacecraft Data, *ISSI Sci. Rep. SR- 001*, edited by G. Paschmann and P. W. Daly, p. 221, Springer, New York.

Lepping, R. P., Jones, J. A., & Burlaga, L. F. (1990). Magnetic field structure of interplanetary magnetic clouds at 1 AU. *Journal of Geophysical Research, 95*(A8), 11957. https://doi.org/10.1029/ja095ia08p11957.

Lundquist, S. (1950), Magneto-hydrostatic fields. *Ark. Fys., 2*, 316 – 365.

Moldwin, M. B., & Hughes, W. J. (1991). Plasmoids as magnetic flux ropes. *Journal of Geophysical Research: Space Physics, 96*(A8), 14051–14064. https://doi.org/10.1029/91ja01167.

Nishida, A. (1994). The Geotail Mission. *Geophysical Research Letters, 21*(25), 2871–2873. https://doi.org/10.1029/94gl01223.

Pollock, C., Moore, T., Jacques, A., Burch, J., Gliese, U., Saito, Y., … Zeuch, M. (2016). Fast Plasma Investigation for Magnetospheric Multiscale. *Space Science Reviews, 199*(1–4), 331–406. https://doi.org/10.1007/s11214-016-0245-4.

Rong, Z. J., Wan, W. X., Shen, C., Zhang, T. L., Lui, A. T. Y., Wang, Y., … Zong, Q.-G. (2013). Method for inferring the axis orientation of cylindrical magnetic flux rope based on single-point measurement. *Journal of Geophysical Research: Space Physics, 118*(1), 271–283. https://doi.org/10.1029/2012ja018079.

Russell, C. T., & Elphic, R. C. (1979). ISEE observations of flux transfer events at the dayside magnetopause. *Geophysical Research Letters, 6*(1), 33–36. https://doi.org/10.1029/gl006i001p00033.

Russell, C. T., Anderson, B. J., Baumjohann, W., Bromund, K. R., Dearborn, D., Fischer, D., et al. (2016). The Magnetospheric Multiscale magnetometers. *Space Science Reviews, 199*(1-4), 189–256. https://doi.org/10.1007/s11214-014-0057-3.

Schindler, K. (1974). A theory of the substorm mechanism. *Journal of Geophysical Research, 79*(19), 2803–2810. https://doi.org/10.1029/ja079i019p02803.

Shen, C., Li, X., Dunlop, M., Liu, Z. X., Balogh, A., Baker, D. N., Hapgood, M., & Wang, X. (2003). Analyses on the geometrical structure of magnetic field in the current sheet based on cluster measurements. *Journal of Geophysical Research: Space Physics, 108*(A5). https://doi.org/10.1029/2002ja00.

Shen, C., Li, X., Dunlop, M., Shi, Q. Q., Liu, Z. X., Lucek, E., & Chen, Z. Q. (2007). Magnetic field rotation analysis and the applications. *Journal of Geophysical Research: Space Physics, 112*(A6). https://doi.org/10.1029/2005ja011584.

Shi, Q. Q., Shen, C., Pu, Z. Y., Dunlop, M. W., Zong, Q.-G., Zhang, H., … Balogh, A. (2005). Dimensional analysis of observed structures using multipoint magnetic field measurements: Application to Cluster. *Geophysical Research Letters, 32*(12). https://doi.org/10.1029/2005gl022454.

Shi, Q. Q., Tian, A. M., Bai, S. C., Hasegawa, H., Degeling, A. W., Pu, Z. Y., … Liu, Z. Q. (2019). Dimensionality, Coordinate System and Reference Frame for Analysis of In-Situ

543 Space Plasma and Field Data. *Space Science Reviews, 215*(4).
544 https://doi.org/10.1007/s11214-019-0601-2.
545 Slavin, J. A. (2003a). Geotail observations of magnetic flux ropes in the plasma sheet. *Journal of*
546 *Geophysical Research, 108*(A1). https://doi.org/10.1029/2002ja009557.
547 Slavin, J. A., Lepping, R. P., Gjerloev, J., Goldstein, M. L., Fairfield, D. H., Acuna, M. H., …
548 Bosqued, J. M. (2003b). Cluster electric current density measurements within a magnetic
549 flux rope in the plasma sheet. *Geophysical Research Letters, 30*(7).
550 https://doi.org/10.1029/2002gl016411.
551 Sonnerup, B. U. Ö., and M. Scheible (1998), Minimum and maximum variance analysis, in
552 Analysis Methods for Multi-Spacecraft Data, *ISSI Sci. Rep. no. SR-001*, edited by G.
553 Paschmann and P. W. Daly, chap. 8, pp. 185–220, European Space Agency, Noordwijk,
554 Netherlands.
555 Sun, W. J., Slavin, J. A., Tian, A. M., Bai, S. C., Poh, G. K., Akhavan-Tafti, M., … Burch, J. L.
556 (2019). MMS Study of the Structure of Ion-Scale Flux Ropes in the Earth's Cross-Tail
557 Current Sheet. *Geophysical Research Letters, 46*(12), 6168–6177.
558 https://doi.org/10.1029/2019gl083301.
559 Wang, R., Lu, Q., Nakamura, R., Huang, C., Du, A., Guo, F., … Wang, S. (2015). Coalescence
560 of magnetic flux ropes in the ion diffusion region of magnetic reconnection. *Nature Physics,*
561 *12*(3), 263–267. https://doi.org/10.1038/nphys3578.
562 Xiao, C. J. (2004). Inferring of flux rope orientation with the minimum variance analysis
563 technique. *Journal of Geophysical Research, 109*(A11).
564 https://doi.org/10.1029/2004ja010594.
565 Yang, Y. Y., Shen, C., Zhang, Y. C., Rong, Z. J., Li, X., Dunlop, M., … Rème, H. (2014). The
566 force-free configuration of flux ropes in geomagnetotail: Cluster observations. *Journal of*
567 *Geophysical Research: Space Physics, 119*(8), 6327–6341.
568 https://doi.org/10.1002/2013ja019642.
569 Zhang, T. L., Baumjohann, W., Teh, W. L., Nakamura, R., Russell, C. T., Luhmann, J. G., …
570 Balikhin, M. (2012). Giant flux ropes observed in the magnetized ionosphere at Venus.
571 *Geophysical Research Letters, 39*(23). https://doi.org/10.1029/2012gl054236.
572 Zhang, Y. C., Z. X. Liu, C. Shen, A. Fazakerley, M. Dunlop, H. Rème, E. Lucek, A. P. Walsh,
573 and L. Yao (2007), The magnetic structure of an earthward-moving flux rope observed by
574 Cluster in the near-tail, *Annales Geophysicae, 25*(7), 1471–1476.
575 Zhao, C., Russell, C. T., Strangeway, R. J., Petrinec, S. M., Paterson, W. R., Zhou, M., … Wei,
576 H. Y. (2016). Force balance at the magnetopause determined with MMS: Application to
577 flux transfer events. *Geophysical Research Letters, 43*(23), 11,941-11,947.
578 https://doi.org/10.1002/2016gl071568.
579 Zhao, J. T., Sun, W. -J., Zong, Q. G., Slavin, J. A., Zhou, X. Z., Dewey, R. M., … Raines, J. M.
580 (2019). A Statistical Study of the Force Balance and Structure in the Flux Ropes in
581 Mercury's Magnetotail. *Journal of Geophysical Research: Space Physics, 124*(7), 5143–
582 5157. https://doi.org/10.1029/2018ja026329.
583 Zhao, Y., Wang, R., & Du, A. (2016). Characteristics of field-aligned currents associated with
584 magnetic flux ropes in the magnetotail: A statistical study. *Journal of Geophysical Research:*
585 *Space Physics, 121*(4), 3264–3277. https://doi.org/10.1002/2015ja022144.
586 Zhou, M., Berchem, J., Walker, R. J., El-Alaoui, M., Deng, X., Cazzola, E., … Burch, J. L.
587 (2017). Coalescence of Macroscopic Flux Ropes at the Subsolar Magnetopause:

588 Magnetospheric Multiscale Observations. *Physical Review Letters, 119*(5).
589 https://doi.org/10.1103/physrevlett.119.055101.
590 Zhou, X.-Z., Zong, Q.-G., Pu, Z. Y., Fritz, T. A., Dunlop, M. W., Shi, Q. Q., … Wei, Y. (2006).
591 Multiple Triangulation Analysis: another approach to determine the orientation of magnetic
592 flux ropes. *Annales Geophysicae, 24*(6), 1759–1765.
593 https://doi.org/10.5194/angeo-24-1759-2006.
594
595
596

Figure1.

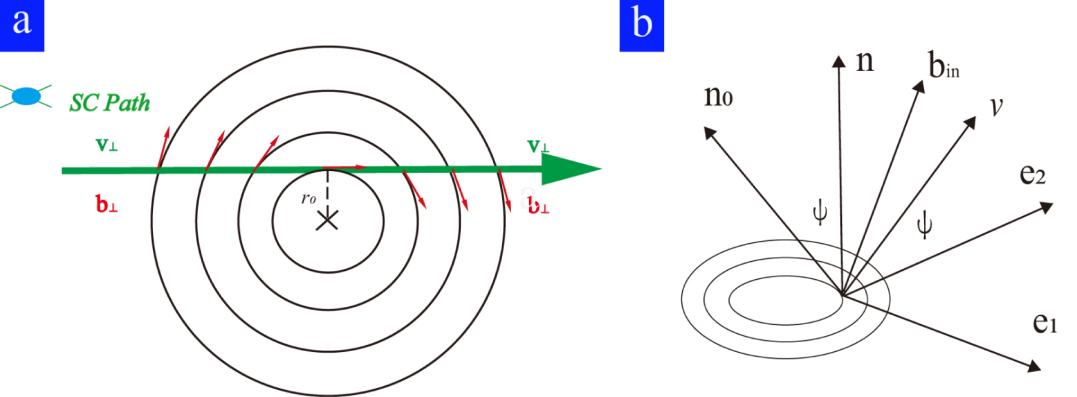
a
SC Path
v⊥
v⊥
b⊥
b⊥
r0
b
n0
n
bin
v
e2
ψ
ψ
e1

Figure2.

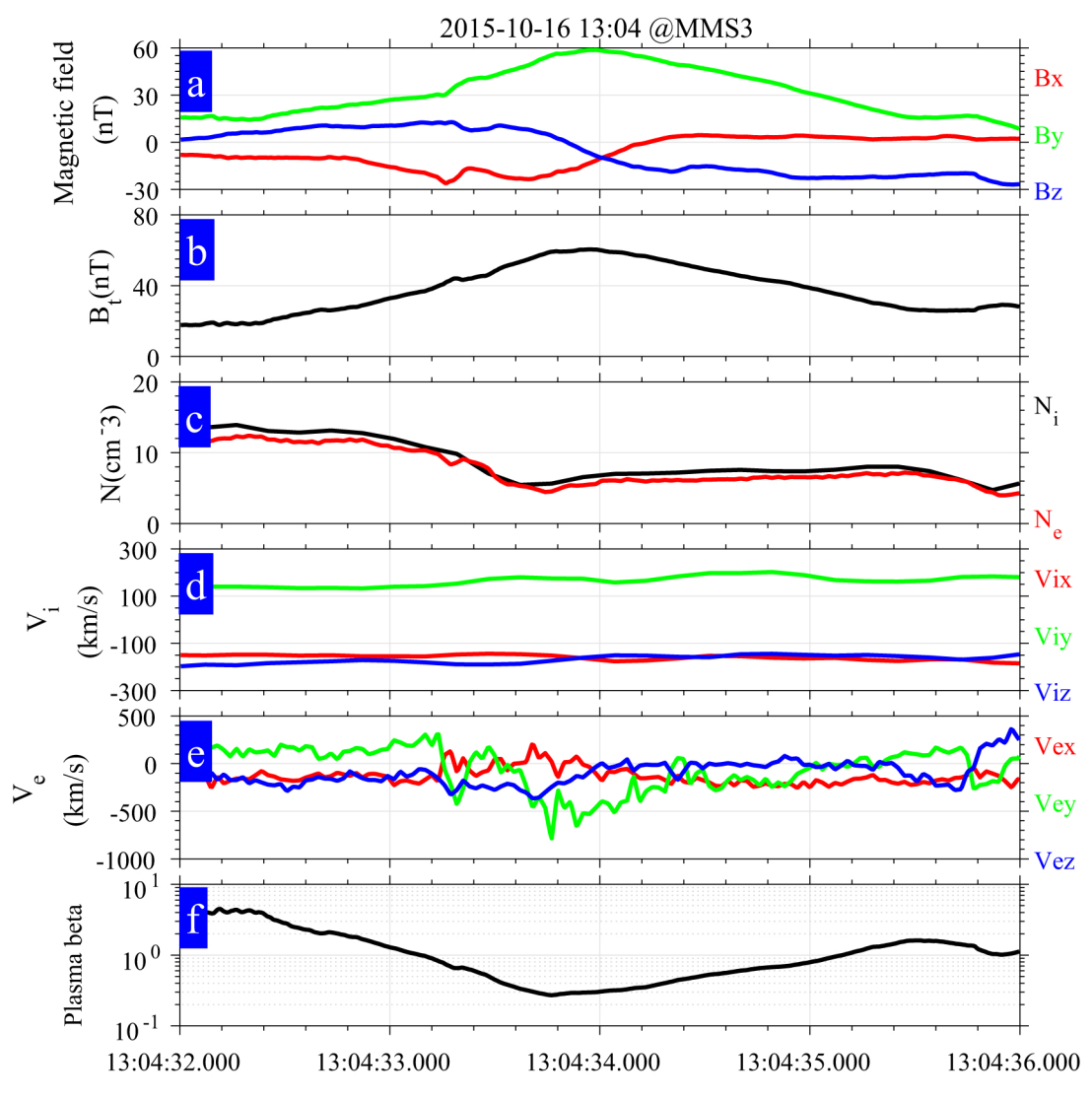
2015-10-16 13:04 @MMS3
Magnetic field (nT)
a
Bx
By
Bz
60
30
0
-30
b
B_t(nT)
80
40
0
c
N(cm^-3)
N_i
N_e
20
10
0
d
V_i (km/s)
Vix
Viy
Viz
300
100
-100
-300
e
V_e (km/s)
Vex
Vey
Vez
500
0
-500
-1000
f
Plasma beta
10^1
10^0
10^{-1}
13:04:32.000
13:04:33.000
13:04:34.000
13:04:35.000
13:04:36.000

Figure3.

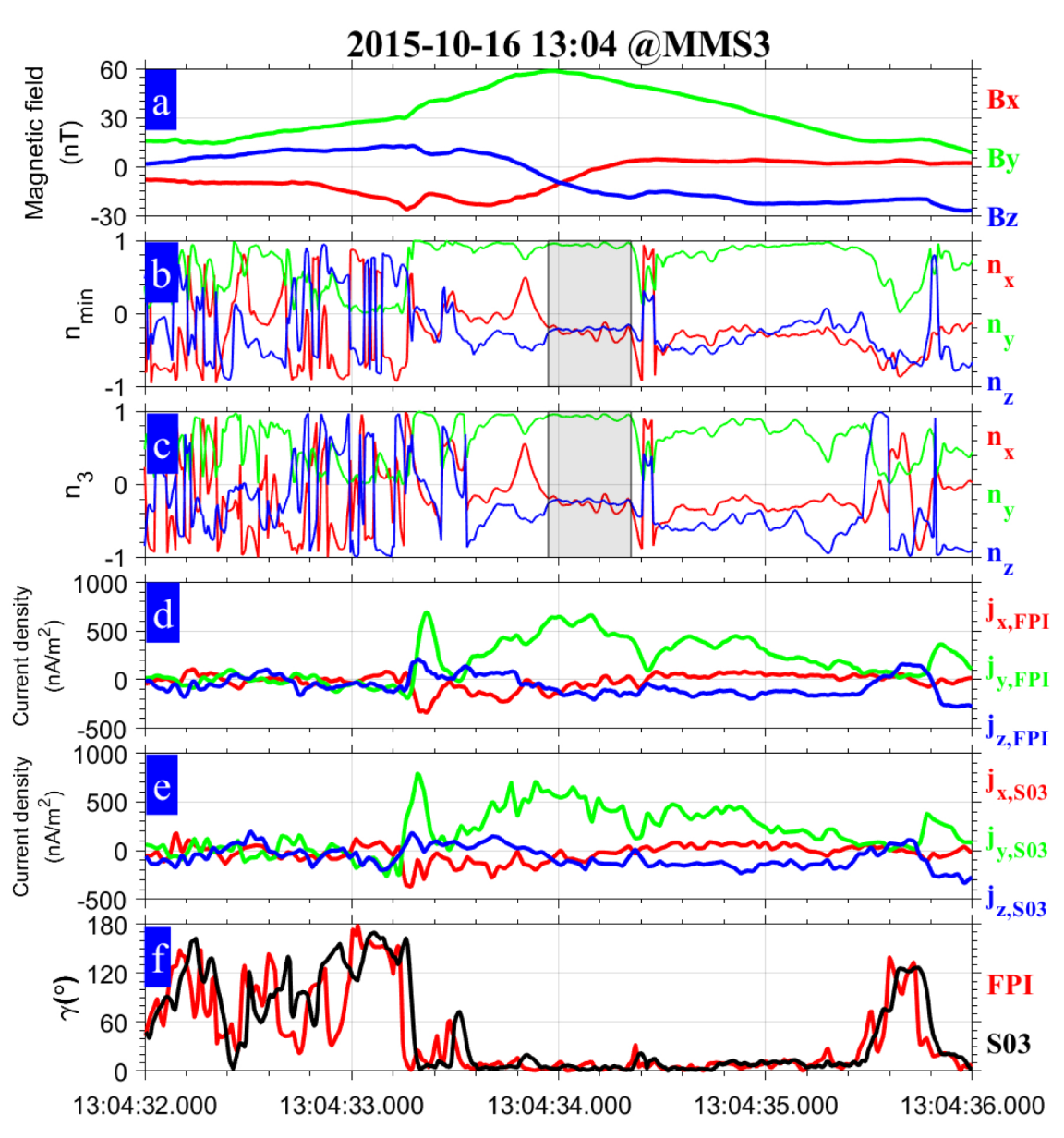
2015-10-16 13:04 @MMS3
a
Magnetic field (nT)
60
30
0
-30
Bx
By
Bz
b
n_{min}
1
0
-1
n_x
n_y
n_z
c
n_3
1
0
-1
n_x
n_y
n_z
d
Current density (nA/m^2)
1000
500
0
-500
$j_{x,FPI}$
$j_{y,FPI}$
$j_{z,FPI}$
e
Current density (nA/m^2)
1000
500
0
-500
$j_{x,S03}$
$j_{y,S03}$
$j_{z,S03}$
f
γ(°)
180
120
60
0
FPI
S03
13:04:32.000
13:04:33.000
13:04:34.000
13:04:35.000
13:04:36.000

Figure4.

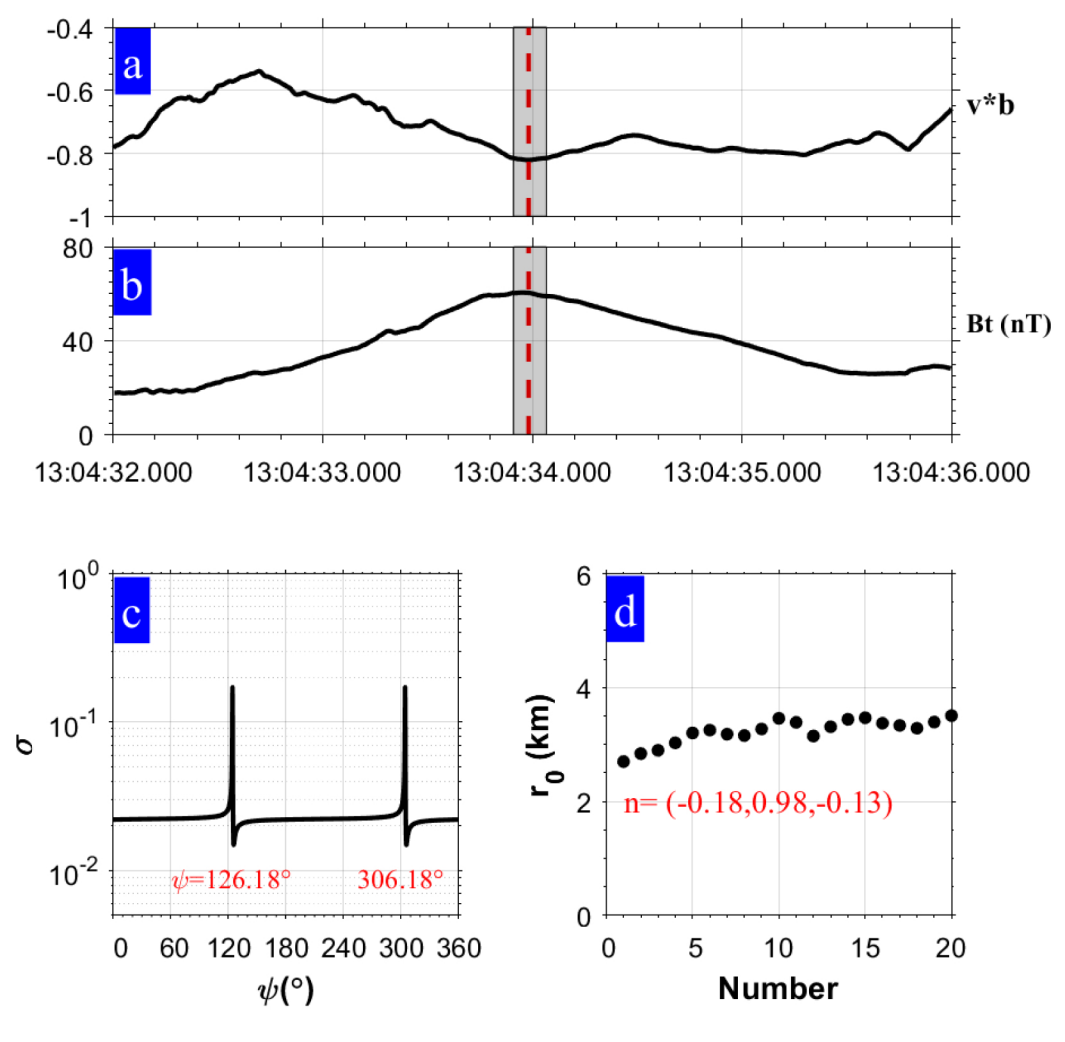
a
b
c
d
v*b
Bt (nT)
-0.4
-0.6
-0.8
-1
80
40
0
13:04:32.000
13:04:33.000
13:04:34.000
13:04:35.000
13:04:36.000
10^0
10^{-1}
10^{-2}
σ
ψ=126.18°
306.18°
0 60 120 180 240 300 360
ψ(°)
6
4
2
0
r_0 (km)
n= (-0.18,0.98,-0.13)
0 5 10 15 20
Number

Figure5.

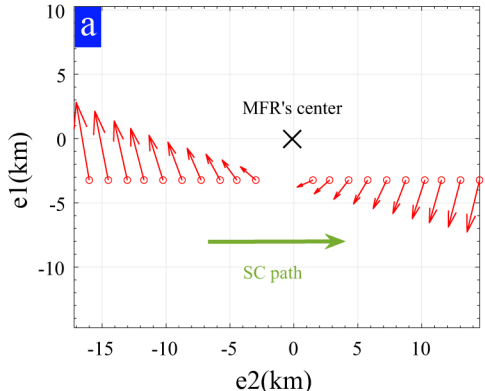
a
MFR's center
SC path
e1(km)
e2(km)
10
5
0
-5
-10
-15
-10
-5
0
5
10

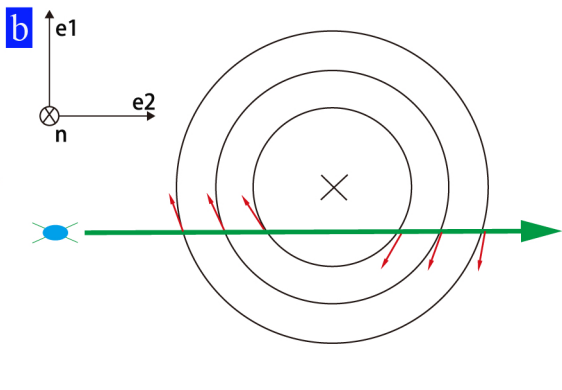
b
e1
e2
n

Figure6.

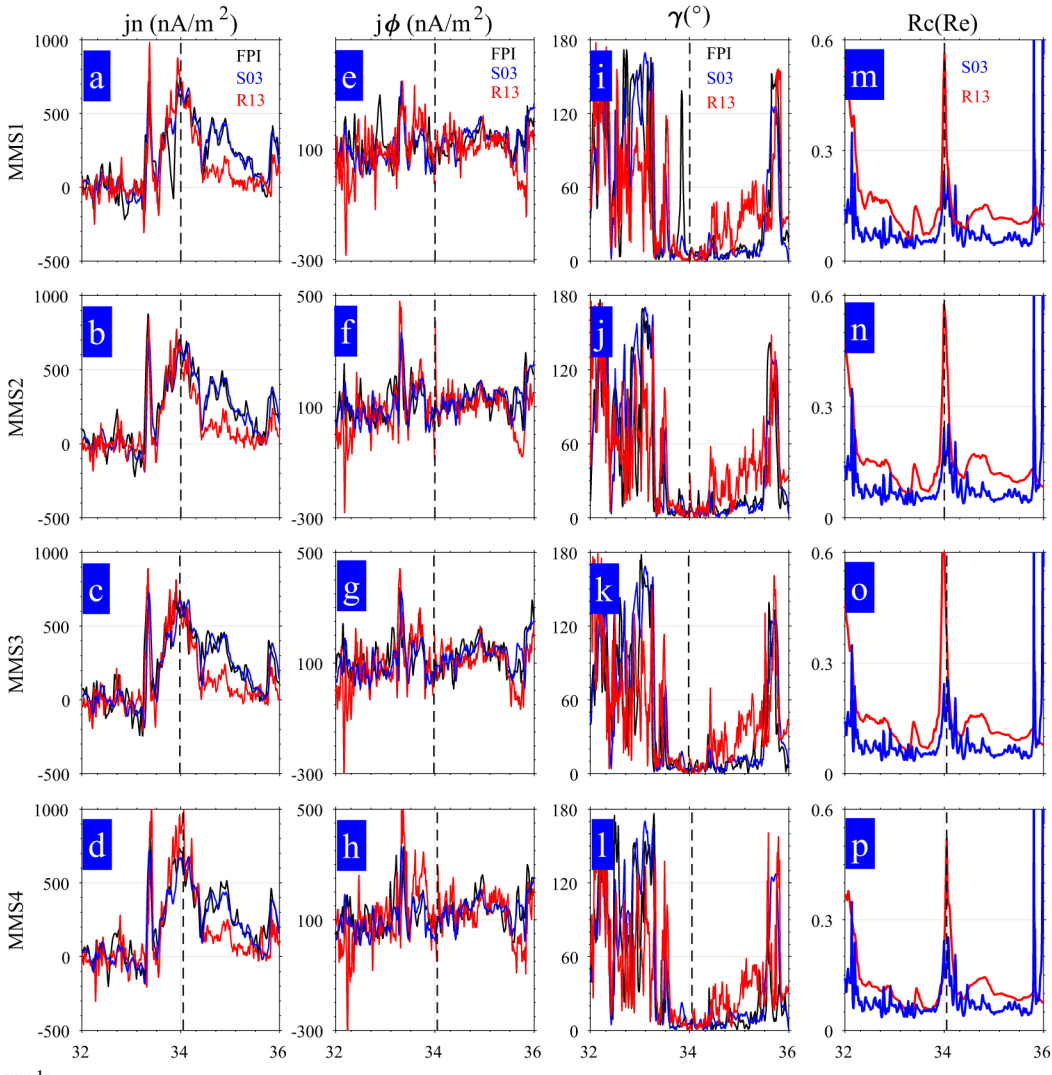

2015-10-16 13:04

Figure7.

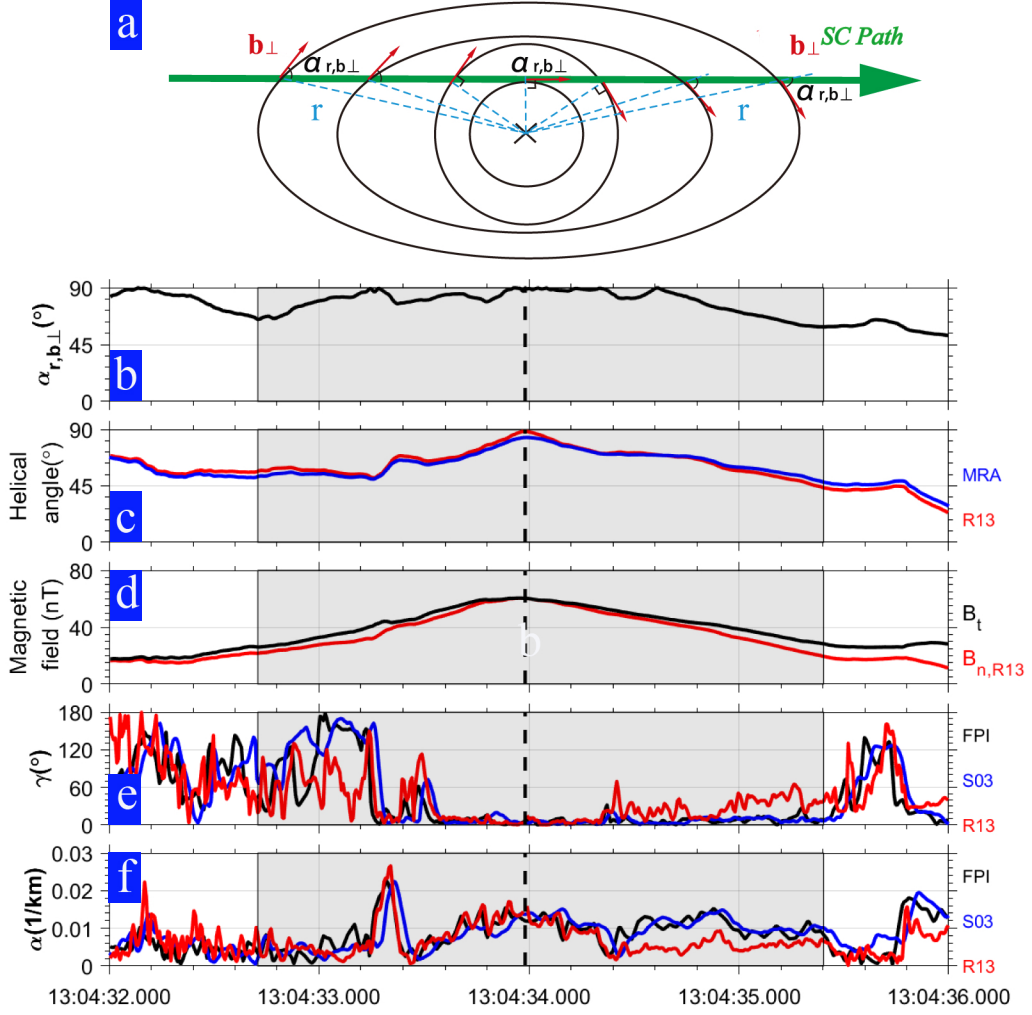
a
b⊥
α r,b⊥
α r,b⊥
b⊥
SC Path
α r,b⊥
r
r
b
α r,b⊥(°)
90
45
0
Helical angle(°)
MRA
R13
Magnetic field (nT)
80
40
B_t
B_n,R13
γ(°)
180
120
60
FPI
S03
R13
α(1/km)
0.03
0.02
0.01
13:04:32.000
13:04:33.000
13:04:34.000
13:04:35.000
13:04:36.000

Figure8.

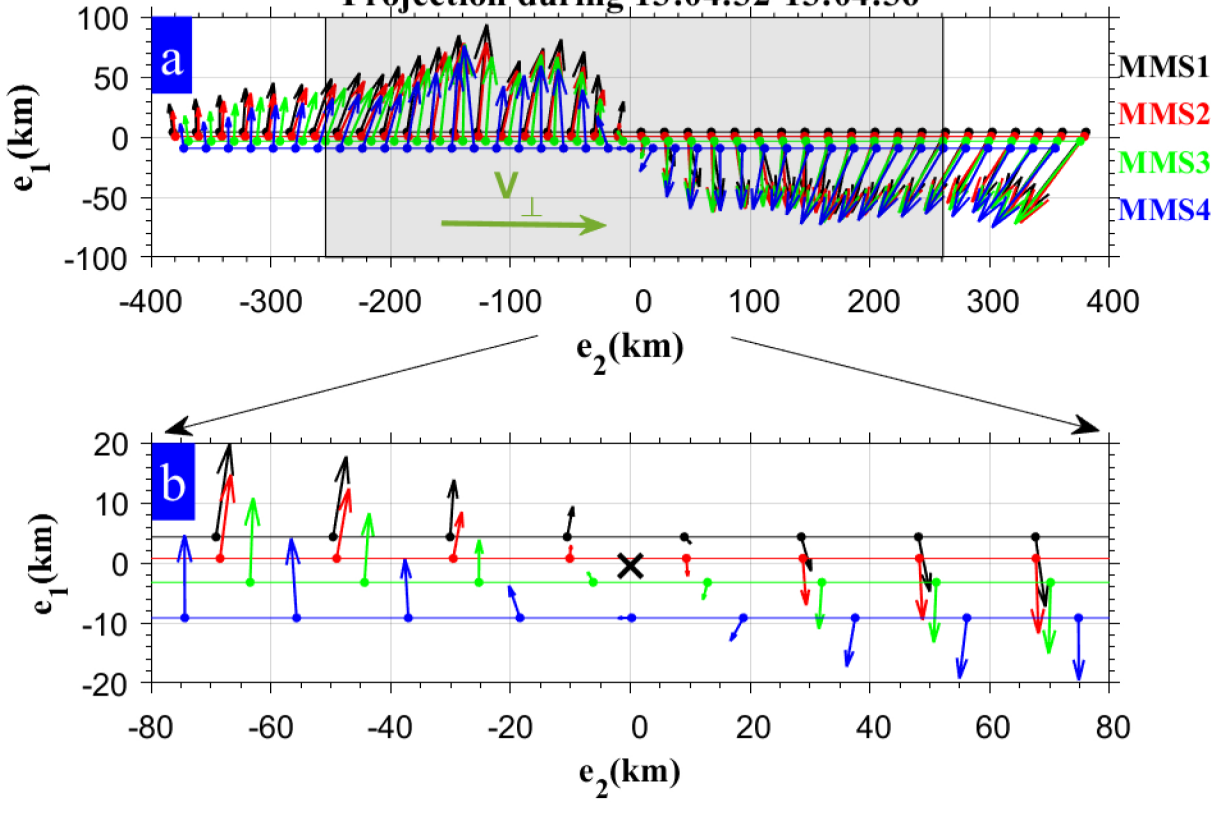
Projection during 13:04:32-13:04:36
a
b
MMS1
MMS2
MMS3
MMS4
$v_\perp$
e_1(km)
e_2(km)
100
50
0
-50
-100
-400
-300
-200
-100
0
100
200
300
400
20
10
0
-10
-20
-80
-60
-40
-20
0
20
40
60
80